More accurate macro-models of solid oxide fuel cells through electrochemical and microstructural parameter estimation - Part I: Experimentation

Published in Journal of Power Sources, Volume 294, 30 October 2015, Pages 658–668

More accurate macro-models of solid oxide fuel cells through electrochemical and microstructural parameter estimation – Part I: Experimentation

Carlos Boigues Muñoz[1,2,*], Davide Pumiglia[2,3], Stephen J. McPhail[2], Dario Montinaro[4], Gabriele Comodi[1], Giulio Santori[5], Maurizio Carlini[3], Fabio Polonara[1]

[1] Dipartimento di Ingegneria Industriale e Scienze Matematiche, Università Politecnica delle Marche, Via Brecce Bianche, Polo Montedago, 60131 Ancona, Italy
[2] UTRINN, ENEA C.R. Casaccia, Via Anguillarese 301, 00123 Rome, Italy
[3] DAFNE, Università degli Studi della Tuscia, Via S. Camilo de Lellis snc, 01100 Viterbo, Italy
[4] SOFCpower SpA, Viale Trento 115/117, 38017Mezzolombardo (Trento), Italy
[5] The University of Edinburgh, School of Engineering, Institute for Materials and Processes, Mayfield Road, The King's Buildings, EH9 3JL, Edinburgh, UK

Abstract

The distributed relaxation times (DRT) method has been employed in order to deconvolute the electrochemical impedance spectroscopy (EIS) measurements carried out on a Ni-YSZ|YSZ|$Pr_2NiO_{4+\delta}$ – GDC solid oxide fuel cell (SOFC). This has enabled to shed light on the diverse physicochemical processes occurring within the aforementioned cell by individuating the characteristic relaxation times of these by means of a specifically designed experimental campaign where temperature and gas compositions in anode and cathode were varied one at a time. A comprehensive equivalent circuit model (ECM) has thus been generated based on the processes observed in the DRT spectra. This ECM has proved to be instrumental for the obtainment of parameters which describe the microstructural and electrochemical properties of the SOFC when used contemporaneously with experimental results and modelling theory (described in Part II of this work).

Keywords: Design of Experiment (DoE); Distributed Relaxation Times (DRT); Equivalent Circuit Model (ECM); SOFC.

1. Introduction

The fact that near future energy scenarios foresee a gradual penetration of solid oxide fuel cells (SOFCs) in the power generation market denotes that this technology is closer than ever in competing face-to-face with traditional powering technologies. However, the existing generation of cells presents a number of drawbacks regarding performance and robustness which could hinder mass commercialization if these still persist in the next generation of SOFCs. Attending to these considerations, the scientific and industrial communities should work hand-in-hand developing improved analysis tools and techniques so to fully understand the degradation phenomena affecting the cells (and ancillaries) enhancing the production of a high-performing, robust and cost-effective product.

Regardless of the fact that significant performance information can be obtained from traditional analysis techniques such as polarization curves and current interruption method, these lack in providing relevant information of the diverse physicochemical processes occurring in the cell (e.g. reaction kinetics, charge transfer, mass transport, Ohmic losses, *etc…),* hence making it hard to pinpoint its criticalities. Electrochemical impedance spectroscopy (EIS) represents a step further to what high quality information it refers as it has the potentiality to shed light on the abovementioned different-nature processes, being each one of them associated to a unique time constant (known as relaxation time) and therefore exhibiting at different characteristic frequencies. However, being such a responsive technique, external instruments and processes – so called electrical artifacts – alter the EIS measurements of the SOFC cell by adding parasitic inductances, therefore an emendation of the measured data must be undertaken so as to minimize their effects. This can done by carrying out an EIS measurement on a specimen with a prominent electrical conductivity (i.e. gold) in the same test station used to characterise the fuel cells and under the same operating conditions and subtracting its spectra to that of the electrochemical cell by means of Eq. (1) and Eq. (2). Figure 1 illustrates a Nyquist plot with the EIS results as measured and the corrected results being evident how the electrical artifacts affect the spectrum in the high frequency region.

$$Z'_{corrected}(\omega) = Z'_{measured}(\omega) - Z'_{gold}(\omega) \quad (1)$$

$$Z''_{corrected}(\omega) = Z''_{measured}(\omega) - Z''_{gold}(\omega) \quad (2)$$

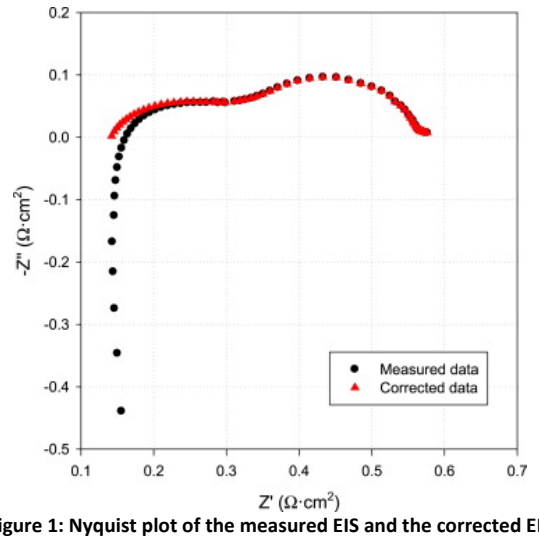

Figure 1: Nyquist plot of the measured EIS and the corrected EIS

Unfortunately this is not the only drawback associated to impedance measurements: due to the high complexity of fuel cells, the responses of the individual physicochemical processes to the EIS excitation signal are often convoluted, hindering in this way their individualization and monitoring. In order to overcome this issue an alternative approach for analyzing impedance spectra has been employed in the present work with a method that allows the calculation of a distribution function of relaxation times and relaxation amplitudes of impedance-related processes from experimental data (DRT method) [1,2].

2. Distributed relaxation times (DRT) method

In the frequency domain and in the discrete form, the SOFC cell's real and imaginary impedances (sum of relaxator terms) can be expressed by means of Eq. (3) and Eq. (4) respectively, both of them linked by means of the Kramers-Kronig relations.

$$Z'(\omega) = R_0 + R_{pol}\sum_m \frac{1}{1+(\omega\tau_m)^2}a_m \tag{3}$$

$$Z''(\omega) = R_{pol}\sum_m \frac{-\omega\tau_m}{1+(\omega\tau_m)^2}a_m \tag{4}$$

where R_0 is the cell's electrical resistance, R_{pol} the polarization resistance, $\omega = 2\pi f$ the angular frequency of the input signal, τ_m the relaxation time of process *m* and a_m is the contribution of process *m* to the total polarization loss.

It is this contribution function which is the cornerstone of the DRT method and it can be obtained either from Eq. (3) or Eq. (4); still, being examples of Fredholm integral equations of the first kind, the inversion of the equation is an ill-posed problem and cannot be solved directly. Even if there are numerous methods which can solve this kind of problems, the most renowned and reliable one is the Tikhonov regularization algorithm which uses a self-consistent regularization parameter [3,4]. In this work the imaginary part of the data has been employed, hence rewriting Eq. (4) in matrix form and introducing the constant value of the polarization resistance into the distribution vector (i.e. $b_m = R_{pol}a_m$) gives:

$$\begin{pmatrix} Z''_1 \\ \vdots \\ \vdots \\ \vdots \\ Z''_m \end{pmatrix} = \begin{pmatrix} \frac{-\omega_1\tau_1}{1+(\omega_1\tau_1)^2} & \cdots & \frac{-\omega_1\tau_m}{1+(\omega_1\tau_m)^2} \\ \vdots & \ddots & \vdots \\ \frac{-\omega_m\tau_1}{1+(\omega_m\tau_1)^2} & \cdots & \frac{-\omega_m\tau_m}{1+(\omega_m\tau_m)^2} \end{pmatrix} \begin{pmatrix} b_1 \\ \vdots \\ \vdots \\ \vdots \\ b_m \end{pmatrix} \tag{5}$$

which for simplicity can be expressed as: $\boldsymbol{Z''} = \boldsymbol{Kb}$.

The Tikhonov regularization foresees the solution of the following minimization problem:

$$\min_{b} \{\|\boldsymbol{Kb} - \boldsymbol{Z''}\|_2^2 + \lambda^2\|\boldsymbol{b}\|_2^2\} \tag{6}$$

where λ is the self-consistent regularization parameter that constrains the smoothness of $\boldsymbol{b}$.

The solution to the previous minimization problem (expressed by means of Eq.(7)) is governed by λ; too small values result in artificial, meaningless peaks while too large values tend to over-smooth the shape of $\boldsymbol{b}$, hence suppressing valuable information.

$$\boldsymbol{b} = (\boldsymbol{K}^T\boldsymbol{K} + \lambda^2\boldsymbol{I})^{-1}\boldsymbol{K}^T\boldsymbol{Z''} \tag{7}$$

where $\boldsymbol{I}$ is the identity matrix.

Various methods have been developed for the optimal selection of regularization parameters (e.g. Discrepancy principle, L-curve, Generalized cross validation method) the L-curve being the most extended one in applied mathematics due to its robustness and ability to treat

perturbations consisting of correlated noise [5,6,7]. The L-curve is basically a trade-off curve between two quantities that ought to be controlled contemporaneously: data fitting and contribution from data errors. On the one hand too large values of lambda tend to over-smooth the shape of the solution curve not fitting well with the given data and hiking the value of the following residual: $\|\boldsymbol{Kb} - \boldsymbol{Z''}\|_2$. On the other hand too small values of the regularization parameter result in a good fit but artificial meaningless peaks will be present in the solution due to the excessive contribution from data errors, thus making $\|\boldsymbol{b}\|_2$ too large (see Fig. 1). Theory states that the optimum value of λ corresponds to the angle of the L-shaped curve, which attending to the figure below – extracted from the experimental data handled in this work – is in the vicinities of $\lambda = 0.01$.

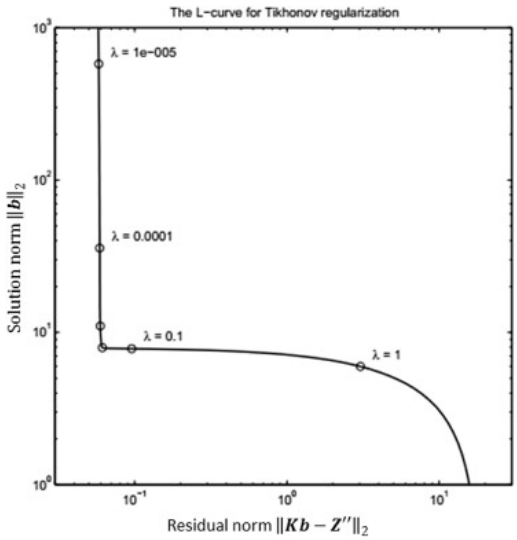

Figure 2: L-curves for the Tikhonov regularization (modified from Ref. [9]).

In this work the Tikhonov regularization algorithm and the optimum value of the regularization parameter have been solved using an in-house program run in MATLAB ®. Nevertheless, there are several commercial and user-free computer programs running on different platforms which allow the solution of the Tikhonov regularization algorithm, for example FTIKREG [8].

Figure 3 illustrates the distribution function (discontinuous line) obtained from the DRT analysis and the imaginary part of the impedance (continuous line) of the Ni-YSZ|YSZ|$Pr_2NiO_{4+\delta}$ - GDC (hereafter PRN) cell. Even if the distribution function is slightly shifted towards the high frequency region when compared to the experimental data, a definite number of peaks tower over the zero line, each of them (or group of them) being the response of a specific physicochemical process. The construction of an equivalent circuit model (ECM) which faithfully models the SOFC is hence straightforward as no *a priori* assumptions were taken into consideration.

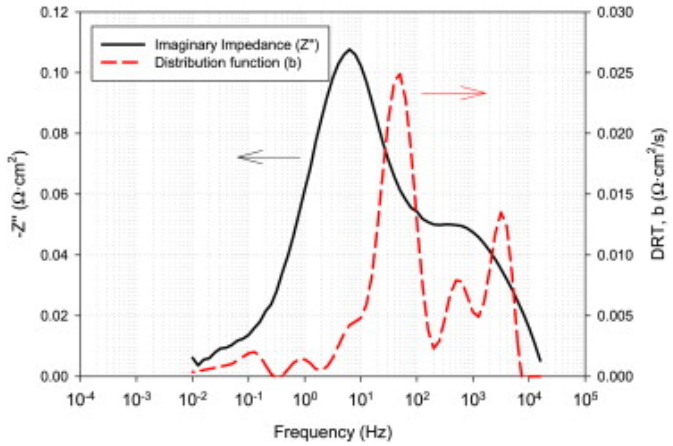

Figure 3: Imaginary component of the PRN cell impedance and the DRT distribution function (λ = 0.01) when the PRN cell is operating at 700 °C under an oxygen partial pressure of 0.21 atm in the cathode and 0.96 atm of H2 and 0.04 atm of H2O in the anode.

3. Experimental procedure

3.1 Equipment setup

The test station employed in the experimental campaign is equipped with a temperature-controlled furnace, mass flow controllers (MFCs) for hydrogen, nitrogen (anode and cathode side), air and oxygen, a bubble humidifier placed in a Julabo UC-5B circulator thermostat (operative range from -20ºC to 100 ºC) in order to humidify the anodic gas flow, an Agilent E3634A DC power supply which can act as a DC electronic load too, an Agilent 34970A data logger and a LABVIEW-based control software. Additionally, the gas pipes connecting the bubble humidifier to the inlet of the SOFC are opportunely enclosed with heating strips so to avoid undesirable steam condensation. For security purposes, the anodic off-gases from the SOFC are directed towards a bubbler with water at room temperature in it – the absence of bubbles alerts of some kind of malfunction in the system. These off-gases are finally guided to the vent which evacuates them to the atmosphere outside the laboratory, whilst the cathodic off-gases, mainly composed of oxygen-depleted air are simply liberated into the atmosphere inside the facilities.

Electrochemical impedance spectroscopy (EIS) measurements were carried out using a Solartron 1287 frequency response analyzer (FRA) module and a Solartron 1260 Impedance/Gain-Phase analyzer. ZView® software for Windows from Scribner Associates Inc. is employed to process the EIS data.

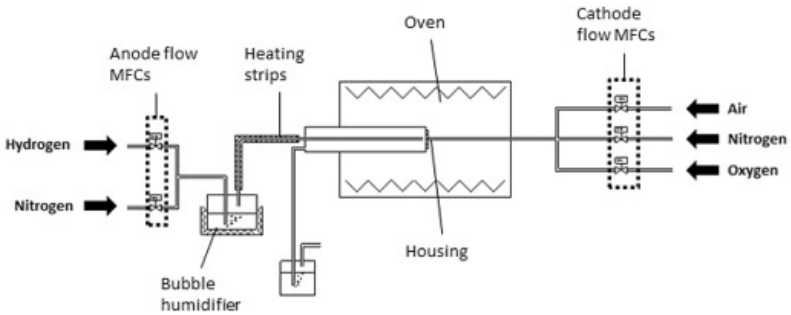

Figure 4: Diagram of the test station.

Electrochemical performance was evaluated on $2cm^2$ active area single cells (see Table 1) mounted on an alumina base and held to it by means of a high-temperature refractory paste which after being baked under the manufacturer's specified conditions plays a dual role: immobilize the cell and block gas leakages from the air chamber to the fuel chamber and *vice versa*. Fine metallic meshes were employed as current collectors, a nickel one at the anode side and a golden one at the cathode side. Figure 3 illustrates the layout of the cell and current collectors in the test bench.

	PRN-cell materials	**Thickness (µm)**
Anode	Ni/8YSZ	500 ± 20
Electrolyte	8YSZ	8 ± 2
Diffusion barrier layer	GDC	4 ± 2
Cathode	$Pr_2NiO_{4+\delta}$	30 ± 10

Table 1: Materials composing the different PRN cell layers and their thicknesses.

3.2 SOFC specimen tested

The Ni-YSZ|YSZ|$Pr_2NiO_{4+\delta}$ – GDC (namely PRN) cell studied in this work was manufactured by SOLIDPOWER S.P.A (Trento, Italy). It must be noted that this cell does not correspond to the manufacturer's standard product which presently incorporates LSCF as cathode. Moreover, the diffusion barrier layer of this cell was developed by ENEA's Materials Department (UTTMAT) utilizing the same commercial GDC powder employed by SOLIDPOWER but adding an extra step in its preparation: the powder was dispersed in aqueous HNO_3 immediately after the removal of residual organic compounds by thermal treatment (internal report –ENEA UTTMAT).

The Ni-YSZ anode was produced by tape casting of water-based NiO/YSZ suspensions, the electrolyte was produced by tape casting of water-based 8YSZ suspensions, the barrier layer (10mol%Gd_2O_2 doped CeO_2) was applied on top of the electrolyte (cathode/electrolyte interface) by screen printing and a further sintering process, whilst the cathode was applied too by screen printing and additionally sintered.

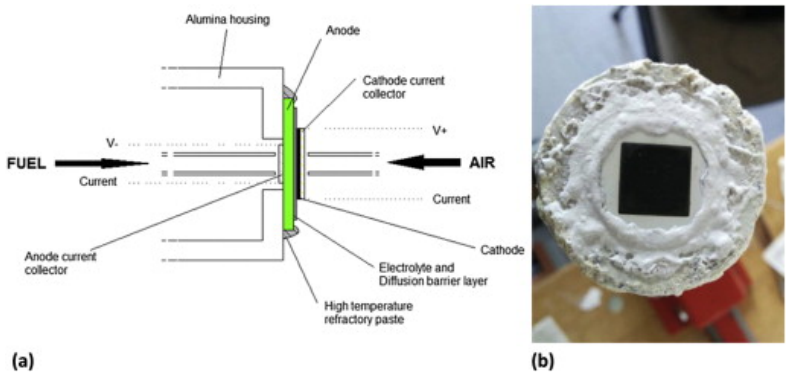

Figure 5: (a) Cross-section diagram of the 2 cm^2 housing. (b) Top-view image of a reduced PRN button cell fixed to the alumina housing.

3.3 Preliminary testing

3.3.1 SOFC cell reduction procedure

PRN cells were reduced at 800ºC under 75 ml/(min·cm^2) of H_2 with 4% humidification to the anode and 150 ml/(min·cm^2) of air to the cathode. Once the cell was fully reduced the first acceptance trials were carried out: if voltage loss was below 5% according to Eq. (8) gas leakage was considered to be negligible and the correspondent cell was valid for further testing. Table 2 illustrates the theoretical Nernst voltage and the experimental data at 800, 750 and 700ºC along with the voltage loss in percentage terms.

$$\Delta E_N(\%) = \frac{E_{N,theoretical} - E_{N,measured}}{E_{N,theoretical}} \cdot 100 \quad (8)$$

where ΔE_N denotes the voltage loss due to leakage, $E_{N,theoretical}$ is the theoretical Nernst voltage and $E_{N,measured}$ is the potential experimentally measured.

Temperature	OCV theoretical value (V)	PRN-cell	
		OCV value (V)	Loss (%)
800°C	1.1008	1.078	2.1
750°C	1.1079	1.091	1.5
700°C	1.1150	1.105	0.9

Table 2: Theoretical and experimental OCV values for the PRN cell at 700, 750 and 800 °C.

3.3.2 Microstructural analysis

In order to analyze the microstructure of the cell, one cell from the batch was cooled down under a reducing atmosphere in the anode (same flows as in the reducing procedure) from the abovementioned reducing temperature down to room temperature with a ramp of 60ºC/h. The cell in its reduced form was then broken into two pieces by mechanical means. Following the same procedure as Tsai *et al*. [9], one of the pieces was allocated for the study of the anodic porous structure whilst the other was employed to analyze the cathode, electrolyte and anode under SEM micrographs.

The cathode and the electrolyte of the first piece were erased by polishing and the resulting sample was then cleaned with distilled water and kept in a dry oven overnight at 120ºC. This sample was then cooled down in dry air down to room temperature and then weighted using a high accuracy balance. Following this first measurement the sample was introduced in a beaker with distilled water and heated up to 100ºC to displace the air from the open pores outside from the structure. After cooling back the water (with the sample in it) down to room temperature the wet cell was weighted. A final measure was carried out by drying the outmost part of the sample leaving its structure completely saturated with water. The porosity value resulting from the Archimedes' method is numerically obtained by means of the following equation:

$$\varepsilon_{an} = \frac{M_{sat} - M_{dry}}{M_{sat} - M_{wet}} \quad (9)$$

SEM micrographs coupled with EDX analysis were performed on the second piece of the sample. The mean radius of the particles, both for anode and cathode, was estimated by analyzing several SEM images employing the free-user software ImageJ [10]. A mean radius of ~ 0.35 µm was estimated for the Ni-YSZ matrix (an identical radius is assumed for the electronic conducting phase and for the ionic conducting phase). Analogously, an average value of 0.35 µm was found for the radii of the cathode particles.

3.3.3 Preliminary electrochemical performance

Polarization curves were carried out under the flows stated by the manufacturer: 75 ml/(min·cm^2) of H_2 humidified at 30ºC (4mol% of H_2O) in the anode and 150 ml/(min·cm^2) of air in the cathode at 800, 750 and 700ºC by applying 50mA every 20 seconds from open circuit voltage (OCV) to 3.3 A (apparatus limit) or until the cell's voltage dropped below 600 mV. Figure 6 illustrates the I-V curves of the PRN cell side by side to those of the manufacturer's standard cell (LSCF cathode); as can be observed the immediate performance of the PRN is significantly higher than that of the LSCF revealing the potentialities of the Ruddlesden-Popper structure as a cathodic material.

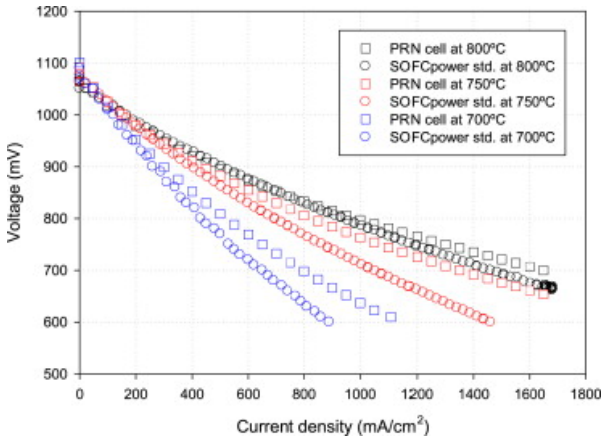

Figure 6: Polarization curves of the PRN cell and the manufacturer's standard cell (LSCF cathode) at 800, 750 and 750 °C.

Impedance spectroscopy measurements were carried out in OCV at 800, 750 and 700ºC with an input voltage amplitude of 10 mV RMS and a frequency range from 100 kHz to 10 mHz. Figure 7 displays the three different EIS measurements in a Nyquist plot elucidating the effect of the temperature on the electrical and polarization resistances. Apart from providing valuable information when compared with EIS data from other cells (such as the LSCF), the main scope of the spectra obtained in the preliminary electrochemical performance phase of the test is to assess the quality of the experimental measurement. This evaluation is carried out by means of the Kramers-Kronig test for Windows [11,12] software developed by B.A. Boukamp *et al*. Figure 8 shows the residual plot of the abovementioned test on the PRN cell (operating at 750ºC) where the maximum error lies below 0.3% indicating that the experimental data impeccably agree with the expected theoretical results.

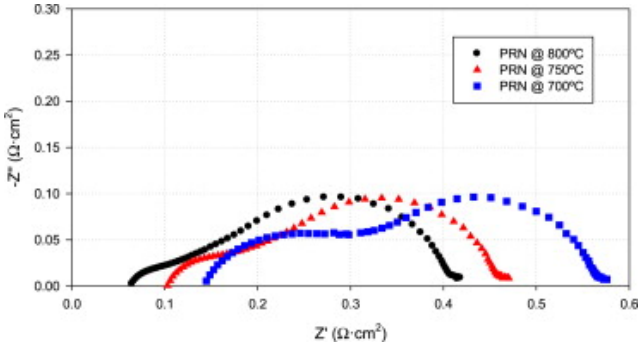

Figure 7: Nyquist plot of the PRN cell at 800, 750 and 700 °C when operating under the preliminary electrochemical performance gas compositions.

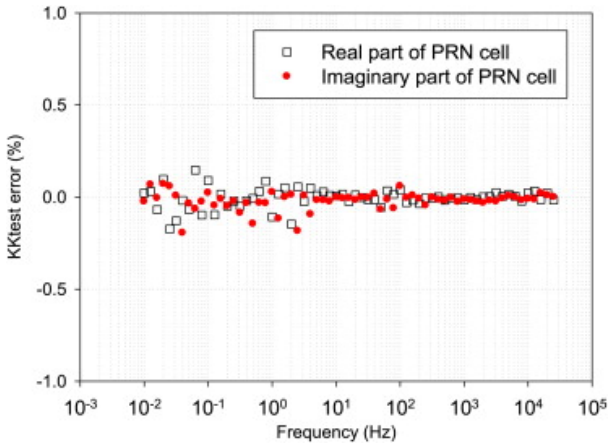

Figure 8: Kramers–Kronig test results for the PRN EIS measurements at 750 °C.

3.4 Physicochemical process identification

In order to elucidate the nature of each peak obtained with the DRT method, the cells were operated under a number of different predefined conditions varying each time one of the following parameters: temperature, anodic gas composition and cathodic gas composition. Table 3 illustrates the partial pressures of cathodic and anodic gas species for all of the tests carried out, which were undertaken at 800, 750 and 700ºC. EIS measurements were performed following the same procedures as explained above.

		pO_2 in cathode (atm)				**pH_2 in anode (atm)**				**pH_2O in anode (atm)**			
		I	**II**	**III**	**IV**	**I**	**II**	**III**	**IV**	**I**	**II**	**III**	**IV**
Cathode gas	pO_2	0.04	0.08	0.21	0.5	0.5	0.5	0.5	0.5	0.5	0.5	0.5	0.5
	pN_2	0.96	0.92	0.79	0.5	0.5	0.5	0.5	0.5	0.5	0.5	0.5	0.5
Anode gas	pH_2	0.96	0.96	0.96	0.96	0.96	0.4	0.2	0.13	0.6	0.6	0.6	0.6
	pH_2O	0.04	0.04	0.04	0.04	0.04	0.04	0.04	0.04	0.04	0.12	0.31	0.4
	pN_2	0	0	0	0	0	0.56	0.76	0.83	0.36	0.28	0.09	0

Table 3: Test matrix containing the molar fractions of the gas species in anode and cathode used for the DRT analysis.

The DRT analysis was performed on the EIS spectra obtained for each operating condition, in this way, by comparing the different curves attained from the test matrix it was possible to associate a peak to a particular physicochemical process. It must be noted that the impedance spectra were beforehand corrected in order to remove the undesirable effects arising from the

electrical artifacts. This was done by carrying out an EIS measurement on a piece of gold with exactly the same area as the active area of the button cells tested and then subtracting its EIS spectrum to that of the electrochemical cell as explained beforehand (Eq. (1) and Eq. (2)).

3.4.1 Hydrogen partial pressure variation in the anode

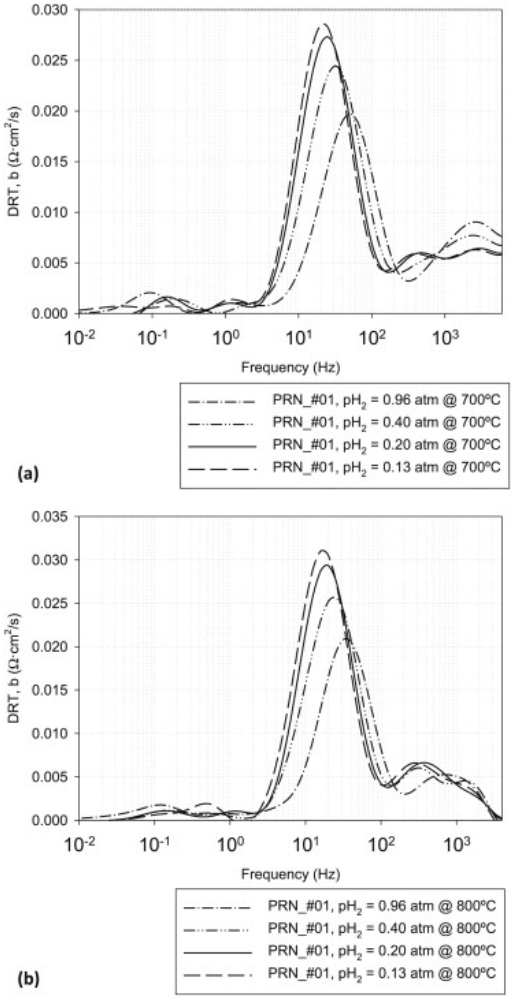

Figure 9: DRT spectra of the PRN cell for hydrogen partial pressure variation at (a) 700 and (b) 800 °C.

3.4.2 Steam partial pressure variation in the anode

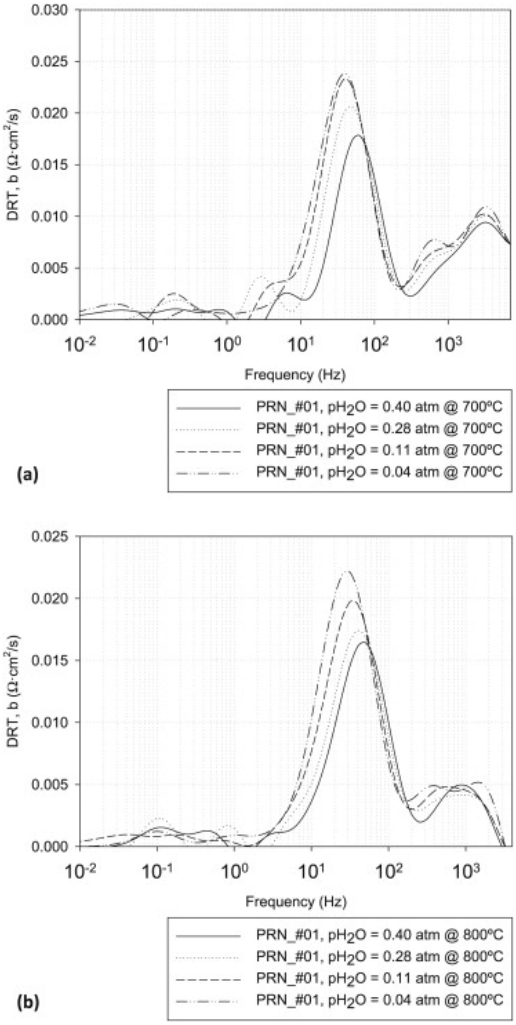

Figure 10: DRT spectra of the PRN cell for hydrogen partial pressure variation at (a) 700 and (b) 800 °C.

3.4.3 Oxygen partial pressure variation in the cathode

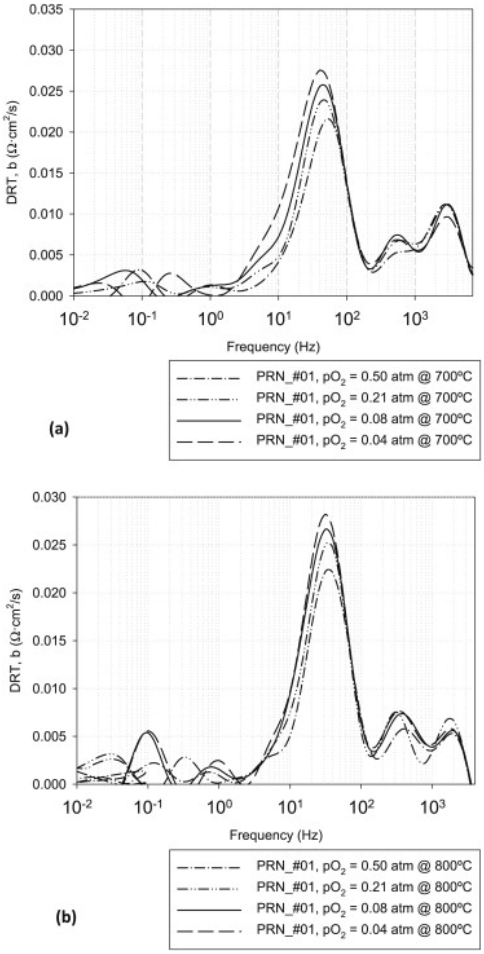

Figure 11: DRT spectra of the PRN cell for oxygen partial pressure variation at (a) 700 °C and (b) 800 °C.

3.4.4 Conclusions

Six different peaks can be identified in the relaxation-time distribution spectra (namely, DRT) of the two types of cells studied in this work (PRN and LSC) according to the figures described previously. Each of the peaks (or group of them) has been associated to a particular physicochemical process occurring within the analysed solid oxide fuel cells.

High characteristic frequencies (>1000 Hz)

The crest covering the highest frequency zone (2000-3000 Hz) is eminently associated to a physicochemical process occurring in the anode since its amplitude is affected by a modification in the anodic gas composition (i.e. pH_2 and pH_2O) and remains unaffected when pO_2 is varied. When confronting Fig. 9 (a) with (b) it seems noticeable how the temperature is the predominant operating parameter affecting the process: the intensity of the peak increases more than 300% (from approximately 0.003 $\Omega \cdot cm^2/s$ in at 800ºC to 0.01 $\Omega \cdot cm^2/s$ at 700ºC) when temperature is decreased by only 100ºC, whilst the impact of gas composition in the summit height is considerably lower. The aforementioned trend is noticeable too in the spectra concerning the steam concentration in the anode, illustrated in Fig. 10, where the variation of pH_2O affects feebly the peak summiting in the highest frequency region, unlike the effect of the operating temperature.

There is strong evidence suggesting that this peak is related to the charge transfer mechanisms occurring in the Ni-YSZ cermet anode. Appendix I illustrates the DRT spectrum of an ideal R-CPE element (Fig. A_I) which is used to model electrochemical phenomena in state-of-the-art SOFC anodes. It can be clearly appreciated that the peak falling in the highest frequency region of all the relaxation-time distribution spectra generated from experimental data has exactly the same form as the theoretical one, thus backing the aforementioned hypothesis. Moreover, besides the experimental data here presented, previous studies determine that anodic charge transfer processes appear in the highest frequency region when H_2 is used as fuel [13].

Intermediate characteristic frequencies (1-1000 Hz)

There are two major peaks summiting in the intermediate frequency region of the relaxation-time distribution spectra and a hump (convoluted peak) in the slowest section of the aforementioned region (more specifically close to a frequency of 8 Hz).

The peak appearing around 300 Hz and that summiting in the 20-30 Hz region have an identical response when pH_2 and pH_2O are modified besides being barely influenced by the operating temperature. This can be observed clearly in the DRT spectra of the PRN cell. It can be said that these peaks have a tight relationship with an anodic process which is barely dependent on the temperature, thus it can be hypothesized that both of them are the consequence of gas diffusion phenomena in the anode. Additionally, modelling theory regarding ECM states that gas diffusion phenomena in porous matrices should be modelled by means of a Finite Length Warburg element, the DRT spectrum of which is shown in Appendix II of this paper (Fig. A_II). The mentioned spectrum shows a dominant peak followed by a series of monotonically decreasing crests at higher frequencies which can perfectly explain the presence of the two peaks observed in the DRT spectra of the PRN cell.

A profound analysis of Fig. 11 reveals that the peak appearing in the 20-30 Hz range and that summiting at 8 Hz (which appears slightly convoluted with the first) are also related to a physicochemical process occurring in the cathode because these are modified when pO_2 is varied. Moreover, it seems that the temperature has a relevant effect on the latter, making it to decrease as the operating temperature increases. From what has just been discussed, it can be said that the dominant charge transfer process in the cathode has a very similar characteristic frequency to that of the gas diffusion phenomena in the anode, hence convoluting to an extent depending on the operating conditions of the SOFCs tested.

Low characteristic frequencies (<1 Hz)

The two peaks appearing in the lowest frequency region can be associated to the diffusion of the cathodic gas in the MIEC porous structure. Even if the quality of the EIS measurements in this region is lower than in the high frequency region (as verified by the Kramers-Kronig test) hence somehow distorting the DRT spectra, it can still be appreciated how these crests are dependent on the oxygen partial pressure in the cathode (Fig. 11 (b)) whilst the temperature plays a secondary role in their variation. Moreover, the gas diffusion of the relatively heavy elements O_2 and N_2 presents the slowest characteristic time of them all which is in line with the experimental results: lowest frequency range. The small intensity of these contributions

can be explained by the slimness of the cathode layer of the tested anode-supported cells (ASC).

Resume

Figure 12 illustrates a generic relaxation-time distribution spectrum of the PRN cell in which the peaks associated to the different physicochemical processes in the cell are comprehensively indicated.

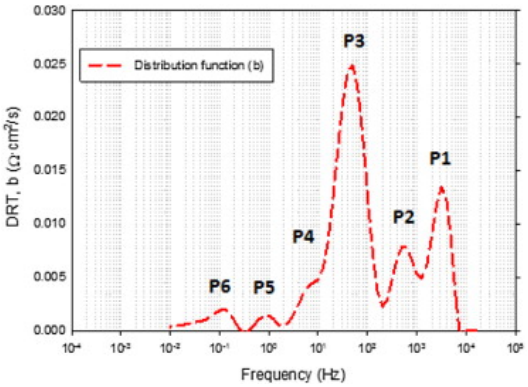

Figure 12: DRT spectra of the PRN cell illustrating the six peaks observed during the experimental campaign.

The table below illustrates the dependencies of each peak with the operating conditions of the SOFC and associates them with a particular physicochemical process.

Peaks	Dependencies				Electrode	Process description
	pH_2	pH_2O	pO_2	Temperature		
P1	Low	Low	No	High	Anode	Charge transfer
P2 + P3	High	High	Low (convolution)	Low	Anode	Gas diffusion
P4	No	No	Low	Medium	Cathode	Charge transfer
P5+P6	No	No	High	Low	Cathode	Gas diffusion

Table 4: Resume of the physicochemical processes occurring in the SOFC and their corresponding peaks in the DRT spectra.

4. Equivalent Circuit Model (ECM)

4.1 Circuit model

Recalling all the considerations proposed for the DRT spectra analysis, the following equivalent circuit model (ECM) has been developed in order to simulate the operation of the fuel cell from the electrochemical point of view (Fig. 13). The circuit may be used with concurrent CNLS fitting of experimental impedance data to estimate the values of circuit elements and thus of the values of the electrochemistry-related parameters characterizing the SOFCs here studied [14].

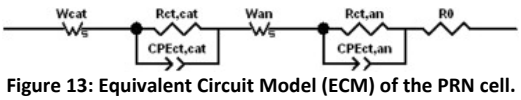

Figure 13: Equivalent Circuit Model (ECM) of the PRN cell.

The electrical resistance of the cell encompasses the electronic and ionic resistances of all the layers composing the SOFC. R_0 is the Ohmic resistance of the cell, which can be regarded as a

sum of the different electronic and ionic resistances within the cell connected in series. The utmost contribution to R_0 is given by the relatively low conductivity of the electrolyte layer, being several orders of magnitude smaller than that of the electrodes.

Conventionally, an RC element is employed to model the EIS response to a charge transfer occurring at the interface of the TPB. Furthermore, when the process takes place in non-ideal conditions: distributed surface reactivity, surface inhomogeneity, roughness or fractal geometry, a constant phase element (CPE) is generally preferred over the capacitor for fitting purposes as it can represent the deviation from a pure capacitance of the EIS response by means of an exponential factor, n, with $0 \leq n \leq 1$ [15]. $R_{ct,an}$ and $R_{ct,cat}$ are the charge transfer resistances at the anode TPB and cathode TPB respectively while $CPE_{ct,an}$ and $CPE_{ct,cat}$ are the double-layer capacitances at the electrical conducting phase and ionic conducting phase interfaces in anode and cathode respectively.

The diffusion of gaseous species in a solid porous structure is generally modelled by a Finite-length Warburg (FLW) diffusion impedance [16]. In Fig. 13 W_{an} is the Finite Length Warburg element representing the gas diffusion through the anode porous matrix whilst W_{cat} is the analogous element for the cathode.

4.2 Goodness of fit

The validity of the ECM is assessed by means of the residuals between the experimental measurement and the fitted value according to Eq. (10) and Eq. (11); the first takes into consideration the real part of the impedance whilst the second regards its imaginary part.

$$\Upsilon_{Re} = \frac{\left|Z'_{exp} - Z'_{fit}\right|}{\left|Z_{exp}\right|} \tag{10}$$

where Υ_{Re} is the error between the real part of the measured impedance (Z'_{exp}) and the fit value (Z'_{fit}).

$$\Upsilon_{Im} = \frac{\left|Z''_{exp} - Z''_{fit}\right|}{\left|Z_{exp}\right|} \tag{11}$$

where Υ_{Im} is the error between the imaginary part of the measured impedance (Z''_{exp}) and the fit value (Z''_{fit}).

Figure 14 displays the experimental measurements and the complex non-linear least squares (CNLS) fit points of the PRN cell when operating at 700ºC. It can be observed how for every frequency both points have nearly identical results in the Nyquist and Bode plots especially at low and intermediate frequencies. From the Bode plot a slight deviation can be highlighted at very high frequencies (>10^4 Hz), further corroborated by the residuals plot (Fig. 15) where the error passes from an average 0.5% up to an 8% in the highest frequency point. Still, the overall fit is exceptional with an error below 2% for most of the frequency range analysed.

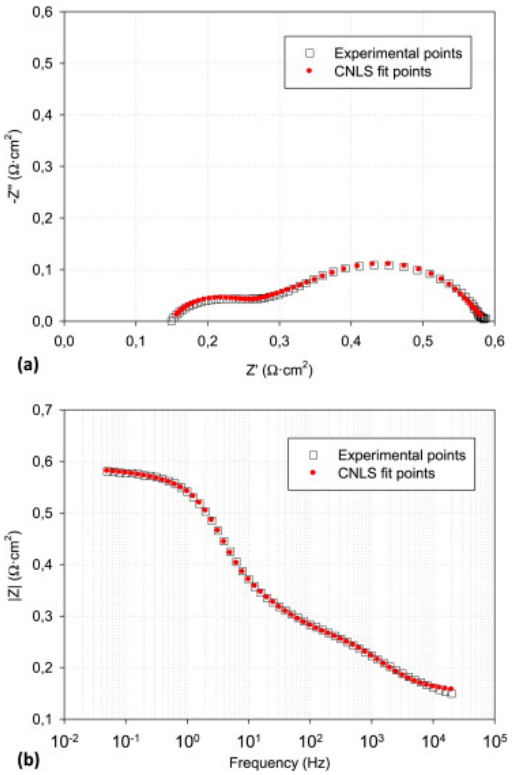

Figure 14: (a) Nyquist and (b) Bode plots of the experimentally obtained EIS points and of the CNLS-fit at 700 °C using the ECM displayed in Fig. 13.

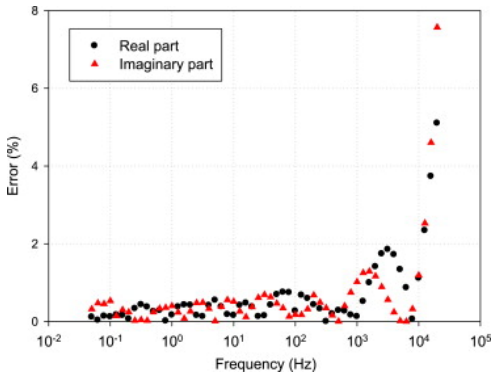

Figure 15: Residuals plot between the experimental measurements and the CNLS fit points at 700 °C.

5. Conclusions

The theory behind the distribution relaxation times (DRT) method and the experimental campaign here addressed have been instrumental for the generation of a comprehensive and robust equivalent circuit model (ECM). Nevertheless, it must be noted that the analysis of the DRT spectra is not a completely straightforward methodology in the sense that some results may induce to errors if the individual signals of the processes are not completely deconvoluted (i.e. when the relaxation times of these lie very close to each other) such as the cathodic charge transfer mechanisms and the anodic gas diffusion mechanism. As discerned in Part II of this work, the above described experimental methodology needs to be supported with complementary analysis techniques and methods, such as the four-point measurement to obtain the electrical conductivities of the cell's different layers, or FIB-SEM imaging to obtain more accurate values of the microstructures. Withal, this methodology is regarded as the base

on which future models (not only CFD) must rest to finally start predicting satisfactorily performance degradation in SOFC cells and components.

Acknowledgements

This work was partially supported by the European Commission through the FP7 Infrastructures Programme, Grant Agreement 284522 (H2FC Infrastructures).

Appendix I

This appendix contains the DRT plots of ideal R-CPE elements.

The theoretical impedance of the resistance is expressed by the following equation:

$$Z_R = R \tag{AI.1}$$

where R is the resistance.

The theoretical impedance of the constant phase element (CPE) element is expressed by the following equation [17]:

$$Z_{CPE} = \frac{1}{C_{CPE}}(j\omega)^{-n} \tag{AI.2}$$

where C_{CPE} is a constant, ω the angular frequency, n an exponent which deviates the CPE element from an ideal capacitor (case $n = 1$) and j the imaginary number.

	R	***C_{CPE}***	***n***
Case 1	0.01	0.005	1
Case 2	0.01	0.005	0.8
Case 3	0.01	0.01	1
Case 4	0.01	0.01	0.8

Table A_I: Nominal values of an R-CPE element according to the fit of numerous experimental results (see Part II).

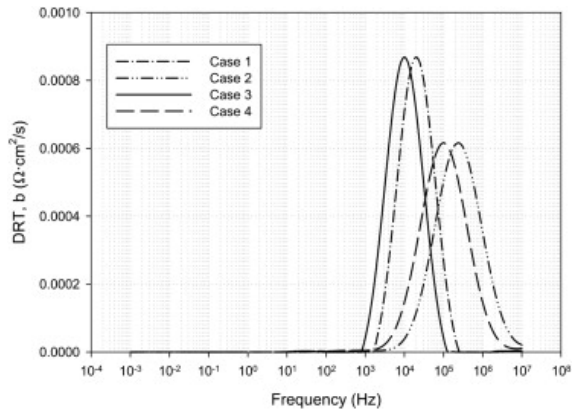

Figure A_I: DRT spectra for an R-CPE element with the values tabulated in Table A_I.

Appendix II

This appendix contains the DRT plots of ideal Finite Length Warburg elements.

The theoretical impedance of the Finite Length Warburg (FLW) element is expressed by means of the following equation [18]:

$$Z_{FLW} = R\frac{\tanh[(jC_{FLW}\omega)^{0.5}]}{(jC_{FLW}\omega)^{0.5}} \quad \text{(AII.1)}$$

Where R is a constant, C_{FLW}, is a second constant, ω the angular frequency and j the imaginary number.

	R	C_{FLW}
Case 1	0.02	0.005
Case 2	0.02	0.01
Case 3	0.02	0.015
Case 4	0.02	0.02

Table A_II: Nominal values of a Finite Length Warburg element according to the fit of numerous experimental results (see Part II).

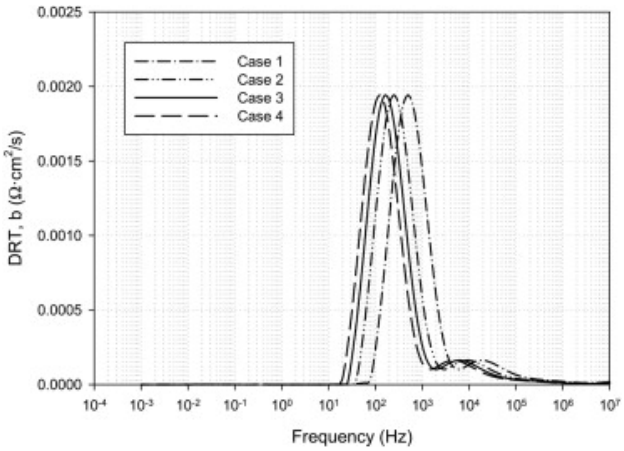

Figure A_II: DRT spectra for a finite length Warburg element with the values tabulated in Table A_II.

Nomenclature

ASC	Anode Supported Cell
a_m	Contribution of physicochemical process *m* to the total polarization
CFD	Computational Fluid Dynamics
CHP	Combined Heat and Power
CNLS	Complex Non-Linear Least Squares
CPE	Constant phase element
DRT	Distributed Relaxation Times
ECM	Equivalent Circuit Model
EIS	Electrochemical Impedance Spectroscopy
E_N	Nernst Potential
FLW	Finite Length Warburg
f	Frequency
GDC	Gadolinium doped ceria

$\boldsymbol{I}$	Identity matrix
$\boldsymbol{K}$	Kernel
M	Weight
MFC	Mass flow controller
OCV	Open circuit voltage
PRN	$Pr_2NiO_{4+\delta}$
R	Resistance
SOFC	Solid Oxide Fuel Cell
T	Temperature
TPB	Triple phase boundary
V	Cell voltage
W_s	Warburg element
x_k	Molar fraction of species *k*
Z'	Real part of impedance
Z''	Imaginary part of impedance

ε	Porosity
λ	Self-consistent regularization parameter for the L-curve
τ_m	Relaxation time of physicochemical process *m*
ω	Angular frequency

References

[1] A.Leonide. *SOFC Modelling and Parameter Identification by means of Impedance Spectroscopy*, PhD Thesis, KIT Scientific Publishing.

[2] N. Link, S.Bauer and B. Ploss. *Analysis of signals from superposed relaxation processes*, J. Appl. Phys. Vol. 69, No. 5, pp. 2759-2767 (1991).

[3] A.N. Tikhonov and V.Y. Arsenin. *Solutions of Ill-Posed Problems*, J. Wiley, New York (1977).

[4] C.W. Groetsch. *The Theory of Tikhonov Regularization for Fredholm equations for the first kind*, Pitman, London (1984).

[5] J. Cullum. *The effective choice of the smoothing norm in regularization*, Math. Comp., Vol. 33, pp. 149-170 (1979).

[6] P.C. Hansen. *Analysis of discrete ill-posed problems by means of the L-curve*, SIAM Review Vol. 34, No. 4 pp. 561-580 (1992).

[7] D. Calvetti, S. Morigi, L. Reichel and F. Sgallari. *Tikhonov regularization and the L-curve for large discrete ill-posed problems*, J. of Computational and Applied Mathematics, Vol. 133, pp. 423-446 (2000).

[8] J. Weese. *A reliable and fast method for the solution of Fredholm integral equations of the first kind based on Tikhonov regularization*, Computer Physics Communications, Vol. 69, pp. 99-111 (1992)

[9] C-L. Tsai and V.H. Schmidt. Tortuosity in anode-supported proton conductive solid oxide fuel cell found from current flow rates and dusty-gas model, J. of Power Sources, Vol. 196, pp. 692-699 (2011).

[10] Rasband, W.S., ImageJ, U. S. National Institutes of Health, Bethesda, Maryland, USA, http://imagej.nih.gov/ij/, 1997-2014.

[11] B.A. Boukamp. *Electrochemical Impedance Spectroscopy in Solid State Ionics; Recent Advances*, Solid State Ionics 169 [1-4] pp. 65-73 (2004).

[12] B.A. Boukamp. A linear Kronig-Kramers Transform Test for Immittance Data Validation, J. Electrochem. Soc. 142 [6], pp. 1885-1894 (1995)

[13] M. Kornely, A. Neumann, N.H. Menzler, A. Leonide, A. Weber and E. Ivers-TIffée. *Degradation of anode supported cell (ASC) performance by Cr-poisoning.* Journal of Power Sources, 196, pp. 7203-7208 (2011).

[14] D.R. Franceschetti and J.R. MacDonald. *Electrode Kinetics, Equivalent Circuits, and System Characterization: Small-Signal Conditions*. J. Electroanal. Chem., 82, pp. 271-301 (1977).

[15] J-B. Jorcin, M.E. Orazem, N. Pébère and B. Tribollet. *CPE analysis by local electrochemical impedance spectroscopy*. Electrochemical Acta, 51, pp. 1473-1479 (2006).

[16] D.R. Franceschetti, J.R. MacDonald and R.P. Buck. *Interpretation of Finite-Length-Warburg-Type Impedances in Supported and Unsupported Electrochemical Cells with Kinetically Reversible Electrodes*. J. Electrochem. Soc., 138 (5), (1991).

[17] J. Bisquert, G. Garcia-Belmonte, P. Bueno, E. Longo and L.O.S. Bulhões. Impedance of constant phase element (CPE)-blocked diffusion in film electrodes. Journal of Electroanalytical Chemistri, 452, pp. 229-234 (1998).

[18] *Tutorial of Zview for Windows*. Scribner Associates Inc.